



Page | 1

# **Aerothermodynamic Flow and Radiation Computations of Surfaces**

Alper Ösün<sup>1</sup>, Christian Mundt<sup>2</sup>

### **Abstract**

Aerodynamic heating remains a critical aspect of hypersonic flight vehicle design. Many experiments in ground-based test facilities and flight experiments have been conducted to determine surface heat fluxes and temperature distribution. In parallel, the advent of high-performance computers and computational techniques permits the calculation of flow physics. Within this study, aerothermodynamic simulation results of an experimental hypersonic vehicle are provided under consideration of radiation heat exchange between solid surfaces at concave regions. The RANS approach is used to solve for the flow field, and a visibility module is coupled with the flow solver to account for radiation effects in concave regions. The resulting delta surface temperature distribution and infrared signatures highlight the significance of the solid surface radiation heat transfer at concave regions for the thermal analysis of hypersonic vehicles.

**Keywords**: *Hypersonic, Aerothermodynamics, Radiation, Heat Transfer* 

## **Nomenclature**

Latin		T	Temperature		
Α	Surface area	t	Time		
CFD	Computational fluid dynamics	u, v, w	Cartesian velocity components		
e	Internal energy	U	Solution vector		
F	Visibility factor	V	Flow velocity vector at a point		
F,G,H	Flux vectors	x, y, z	Cartesian coordinates		
GETHRA General thermal radiation			Greek		
J	Source vector	Δ	Difference		
Ма	Mach Number	ε	Emissivity coefficient		
$q_{\rm gas,w}$	Heat flux in the gas at the wall	$\mathcal{E}_f$	Fictitious emissivity coefficient		
$q_{\rm rad}$	Surface radiation heat flux	Θ	Angle		
r	Distance	ρ	Density		
RANS	Reynolds averaged navier stokes	σ	Stefan-Boltzmann constant		

HiSST-2025-65 Aerothermodynamic Flow and Radiation Computations of Surfaces Copyright © 2025 by author(s)

<sup>&</sup>lt;sup>1</sup> Universität der Bundeswehr München, Faculty of Aerospace Technology, Werner-Heisenberg-Weg 39, 85579 Neubiberg, alper.oesuen@unibw.de

<sup>&</sup>lt;sup>2</sup> Universität der Bundeswehr München, Faculty of Aerospace Technology, Werner-Heisenberg-Weg 39, 85579 Neubiberg, christian.mundt@unibw.de

#### 1. Introduction

Since the beginning of the space age and the development of high-speed vehicle technology, aerodynamic heating of these vehicles garnered considerable interest [1]. The thermal management of hypersonic vehicle surfaces depends on many aspects and plays an essential role in the design of these vehicles. For instance, the heat radiation intensity at specific wavelengths is of significant interest for both military and civilian applications, particularly in the detection and tracking of high-speed vehicles [2].

Experimental investigations in ground-based testing facilities of high-speed vehicles bring numerous challenges. Shock and Ludwieg tube experiments are conducted for a fraction of a second, and they need complicated measurement instrumentation. A further difficulty is replicating the flight environment in ground-based testing facilities, which are limited and challenging. Therefore, research institutes and companies conduct flight experiments to verify the design of hypersonic vehicles. One such example a hypersonic flight experiment, STORT (Key Technologies for High-Speed Return Flights of Launcher Stages), was conducted by the DLR (German Aerospace Center) in 2022 [3]. Besides these experimental investigations, low- and high-fidelity numerical simulations of hypersonic applications deliver benefits for the design phase. For this purpose, CFD (Computational Fluid Dynamics) simulations are a widely accepted general approach to determine flow physics and to transfer wind tunnel results [4]. This technique enables the calculation of relevant flow parameters, such as velocity, pressure, heat flux, etc., acting on the flight vehicle.

The aerodynamic heating phenomenon of hypersonic vehicles results in hot solid body surfaces. Consequently, heated solid body surfaces start radiating significant amounts of energy. This energy will be trapped in concave flight vehicle regions. One such example region is near aerodynamic design features like fins, canards, or wings. This direct radiation influences the surface temperature distribution, and it needs special treatment by a radiation module coupled with CFD solvers. The main objective of this study is the investigation of radiation heat transfer effects in concave hot surface regions in aerother-modynamic analysis of high-speed vehicles.

## 2. Numerical Method

To investigate the flow physics around the selected flight vehicle, the Navier-Stokes Multi Block (NSMB) solver is used [5,6]. NSMB employs the density-based finite volume CFD method, where the flow domain is divided into several structural blocks. Geometry and the mesh are prepared using the CATIA V5 and ANSYS ICEM CFD software, respectively. The computation of radiation heat transfer between surfaces at concave regions is examined using the GETHRA (General Thermal Radiation) module [7].

## 2.1. Solution Procedure

Various meshes have been prepared and, a grid study was carried out to determine efficient models at the beginning. Selected model grids are divided into multiple blocks, and these blocks are distributed to computational cores in a local high-performance computing cluster. Before starting the simulation, the GETHRA module needs to be coupled with the NSMB solver to perform calculations. Within this study, three radiation module simulation configurations are preferred. In the primary configuration, no radiation module is used at all, which would be the reference case. Secondly, radiation computations are directly coupled with the solver, and after every 200 iterations, the GETHRA package computes fictitious emissivity coefficients of solid wall surface elements. NSMB utilizes these computed emissivity coefficients to adjust radiation heat fluxes from the solid wall boundary surfaces. Hence, thermal radiation heat exchange between concave surfaces is considered at interference regions. Lastly, the radiation module is only activated at the end of the first configuration, where the solution is already converged.

#### 2.2. Governing Equations

NSMB solves the 3D flow domain using the unsteady compressible Reynolds Averaged Navier Stokes (RANS) equations in conservation form given in Eq. 1, where t denotes time and x, y, z are the cartesian coordinates. The column vectors F, G, H are the flux terms, J represents a source term, and U is called the solution vector. Elements of U, given in Eq. 2, are the dependent variables that are solved numerically in time steps [4].

$$\frac{\partial U}{\partial t} + \frac{\partial F}{\partial x} + \frac{\partial G}{\partial y} + \frac{\partial H}{\partial z} = J \tag{1}$$

$$U = \begin{cases} \rho \\ \rho u \\ \rho v \\ \rho w \\ \rho \left( e + \frac{V^2}{2} \right) \end{cases}$$
 (2)

For spatial discretization, the second-order upwind scheme is preferred. Hypersonic flows with mixed regimes (from subsonic to hypersonic) can be solved accurately with the AUSM+UP method [8], although this is computationally expensive. The Van Leer type of flux limiter ensures the stability of the results given in this study [9]. Furthermore, the chemical equilibrium modelling of the air is sufficient for the flow field solution, considering the selected vehicle geometry and simulation point of the low hypersonic regime. Therefore, the standard Park's model for air, consisting of 5 species assuming chemical equilibrium, is chosen for this study.

#### 2.3. Turbulence Models

Transition from laminar flow condition to turbulent of a typical near sharp cone nose geometry of a slender body has been extensively researched in past decades [10]. Laminar boundary layer flow brings its advantages, such as reduced surface skin friction and lesser heat flux directed toward the wall. An aerothermodynamic designer of high-speed vehicles intends to delay the laminar-turbulent transition as downstream as possible to benefit from its advantages. The disturbances generated by aerodynamic design features such as canards, fins, and wings could initiate turbulence. Even if there is no external reason, laminar-turbulent transition occurs after the amplification of internal flow disturbances in laminar flow. The exact location where the boundary layer transition begins and ends is difficult to determine, and current methods presume it with uncertainty. Boundary layer stability and transition can be investigated using linear stability theory (LST) and parabolized stability equations (PSE) [11].

Considering the selected high-speed vehicle, turbulence must be considered properly. Canard features at the front body initiate the turbulent flow, even if the flow is laminar until the canard position. In the low-fidelity RANS method, turbulence needs to be modeled. Menter's two-equation k-w shear stress transport model (k-w SST) is favored within this study due to its accuracy and robustness. This model combines the k-e model for free shear flow outside of the boundary layer and k-w model for the inner region of boundary layer. Turbulence kinetic energy and rate of dissipation of the eddies are the two variables calculated in the formulation of k-w SST model [12].

## 2.4. Boundary Conditions

The inlet boundary condition of the simulation is chosen from the high-enthalpy regime of the vehicle mission, and it is given in Table 1. According to the experimental results, it has flown for more than 60 seconds at this regime, and several scientific missions were carried out [3].

Boundary conditions at selected simulation point adopted from [3]. Table 1.

Altitude [km]	Reynolds Number [-]	Mach Number [-]	Ambient Pressure [Pa]	Density [kg/m³]	Ambient Temperature [K]
38	$8.6 \times 10^{6}$	8	400	$0.54 \times 10^{-2}$	250

The radiation adiabatic wall boundary condition is employed for all solid surfaces. The selected boundary condition routine can be described as follows: the convective heat flux of the gas to the wall  $q_{\rm gas,w}$ is balanced through the emitted surface radiation heat flux of the wall,  $q_{\rm rad}$  as given in Eq. 3. Hence, there is no net heat flux into the wall. Consequently, solid surface temperatures can be computed via the Stefan-Boltzmann law. In Eq. 4,  $\sigma$  refers to the Stefan-Boltzmann constant and  $\varepsilon$  is the emissivity of the surface [13].

$$q_{\rm rad,w} = -q_{\rm gas,w} \tag{3}$$

$$q_{\text{rad w}} = \varepsilon \sigma T_{\text{w}}^4 \tag{4}$$

However, the radiation adiabatic wall boundary condition is not sufficient for concave solid surface regions. The radiation heat transfer between the solid surfaces is not taken into account, which causes an underestimation of surface temperatures at concave regions. The GETHRA module defines a variable called fictitious emissivity for each surface panel and computes visibility factors  $F_{12}$  by Eq. 5 [7]. The subscripts in Eq. 5 refer to the surfaces, A is the surface area, r is the distance between two surfaces, and  $\Theta$  is the angle between a surface normal vector and the connecting line of surface centers. Fig. 1 describes a sketch of the concave surface area system with radiation heat transfer elements. The radiation balance  $\Delta q_1$  of the surface  $A_1$ , without considering the reflection effects, is given in Eq. 6. In this equation, the first term on the right-hand side represents the emitted heat flux of the surface  $A_1$ , while the second term corresponds to the absorbed heat flux from the surface  $A_2$ . Accordingly, the emissivity levels of surfaces in concave regions vary. The fictitious emissivity coefficient  $\varepsilon_f$  replaces the surface emissivity  $\varepsilon$  of the panel, resulting in a more realistic temperature distribution compared to the radiation wall boundary condition [13]. Eq. 7 defines the fictitious emissivity coefficient  $\varepsilon_f$  for a panel based on its radiation balance  $\Delta a$ .

$$F_{12} := \frac{1}{A_1} \iint \frac{\cos\Theta_i \cos\Theta_j}{\pi r_{12}} dA_1 dA_2 \tag{5}$$

$$\Delta q_1 = q_1 - q_2 \frac{\varepsilon F_{21}}{dA_1} \tag{6}$$

$$\varepsilon_{f,1} = \frac{\Delta q_1}{\sigma T_1^4} = \frac{q_1 - q_2 \frac{\varepsilon F_{21}}{dA_1}}{\sigma T_1^4} \tag{7}$$

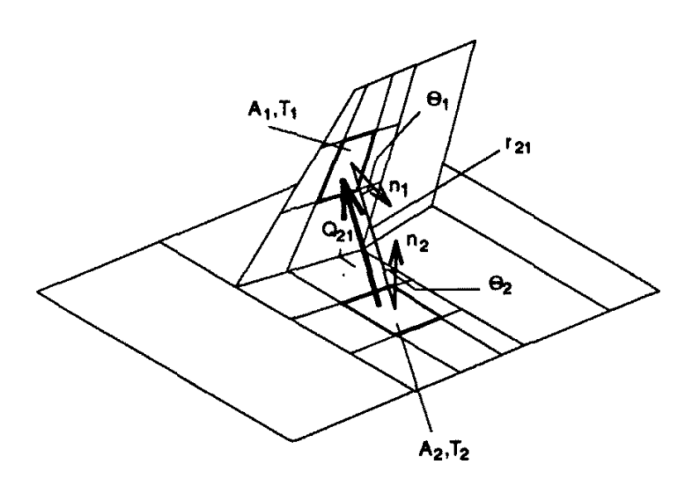
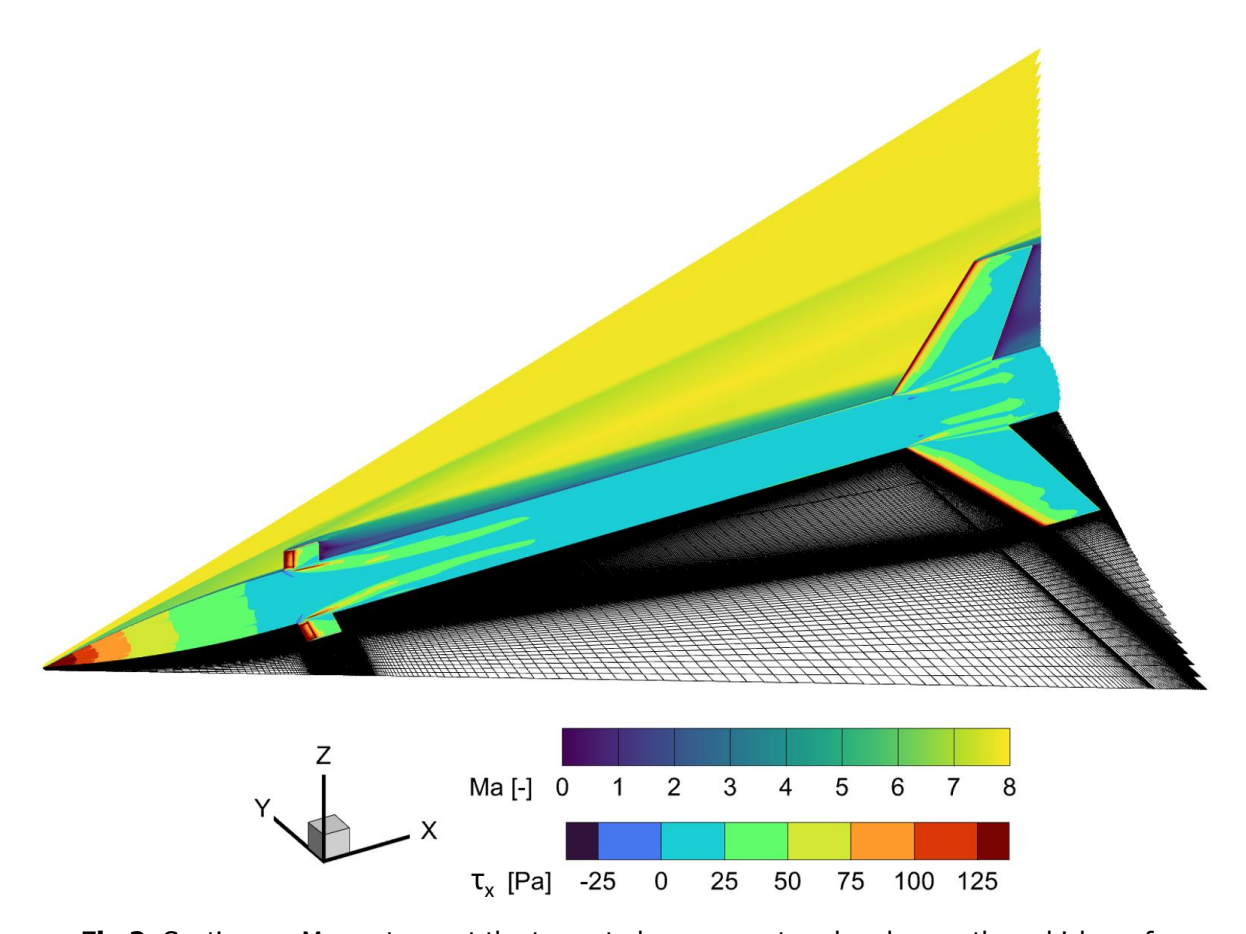


Fig 1. Radiation heat transfer between solid surfaces in a concave region [7].

## 3. Results

The Ma distribution of the flow field, the wall shear stress along the vehicle x-axis  $\tau_x$ , and the mesh grid of the vehicle's last stage shown in Fig. 1. The radiation module is strongly coupled for the results shared in this figure. Wake of the flight vehicle at the very downstream is excluded for visualization purposes. Cut planes in this figure are chosen by considering the mid-plane of canards and wings. In the first cut plane at the top side of the figure, the shock is formed at the rocket tip, and it reaches as an oblique shock until the end of the simulation domain. Similar shock formations are also observed around the design features like canards and wings. Wakes after the canards and wings are also apparent. Over the vehicle solid surface drawn  $\tau_x$  contours inform about the flow physics and characteristics such as horseshoe vortexes and reverse flows. In the second cut plane at the bottom side of the figure, the 2D projection of the 3D structured mesh is given. Around the canards and wings the O-grid strategy is adapted.

HiSST-2025-65 A. Ösün, Ch. Mundt Copyright © 20 The procedure of the dimensionless  $\varepsilon_f$  computation over the solid surface was discussed in Sec. 2.4, where  $\varepsilon_f$  depends on surface panel temperatures and view factors. Therefore, at the strongly coupled radiation module configuration, the  $\varepsilon_f$  is recomputed during the simulation and the  $\varepsilon_f$  distribution over the vehicle converges together with the simulation itself. Fig. 3 demonstrates the GETHRA module computed  $\varepsilon_f$  values with respect to the selected reference emissivity of 0.85. In other words, without considering the concave radiation effects, the standard radiation adiabatic boundary condition assumes the same  $\varepsilon$  as 0.85 all around the vehicle surface. Although concave surface regions of vehicles, such as canards and wings, show decreased  $\varepsilon_f$  down to 0.2 as was expected beforehand.



**Fig 2.** Continuous Ma contours at the top cut plane,  $\tau_x$  contour bands over the vehicle surfaces, and the mesh grid of the vehicle at the bottom cut plane.

A closer view of  $\varepsilon_f$  distribution around the canard and the wing are shown in Fig. 4, where surface panels used by the radiation module are described by the edges. These surface panels are generated by the radiation module using surface elements. To make the  $\varepsilon_f$  computation efficient and less computationally demanding, fine surface elements are grouped and approximated as coarse panels, where 10 nodes in each direction are combined in this case. Then, every computed surface panel  $\varepsilon_f$  is distributed to the corresponding surface elements  $\varepsilon$ . Moreover, the canard feature of the vehicle is qualitatively less streamlined and located upstream compared to the large wing at the end of the vehicle. As a result, the shock forming around the canard has a stronger influence on the vehicle fuselage adjacent to the canard leading edge area compared to the wing. A larger area with lower the  $\varepsilon_f$  values emerged in Fig. 4 (a) than in (c). Moreover,  $\varepsilon_f$  distribution variation between (a) and (b) supports that, without considering the radiation at concave regions during the simulation, the resulting surface temperatures are underestimated. Hence, a more severe  $\varepsilon_f$  distribution is necessary to reach thermal balance, and (b) is the outcome of the radiation module.

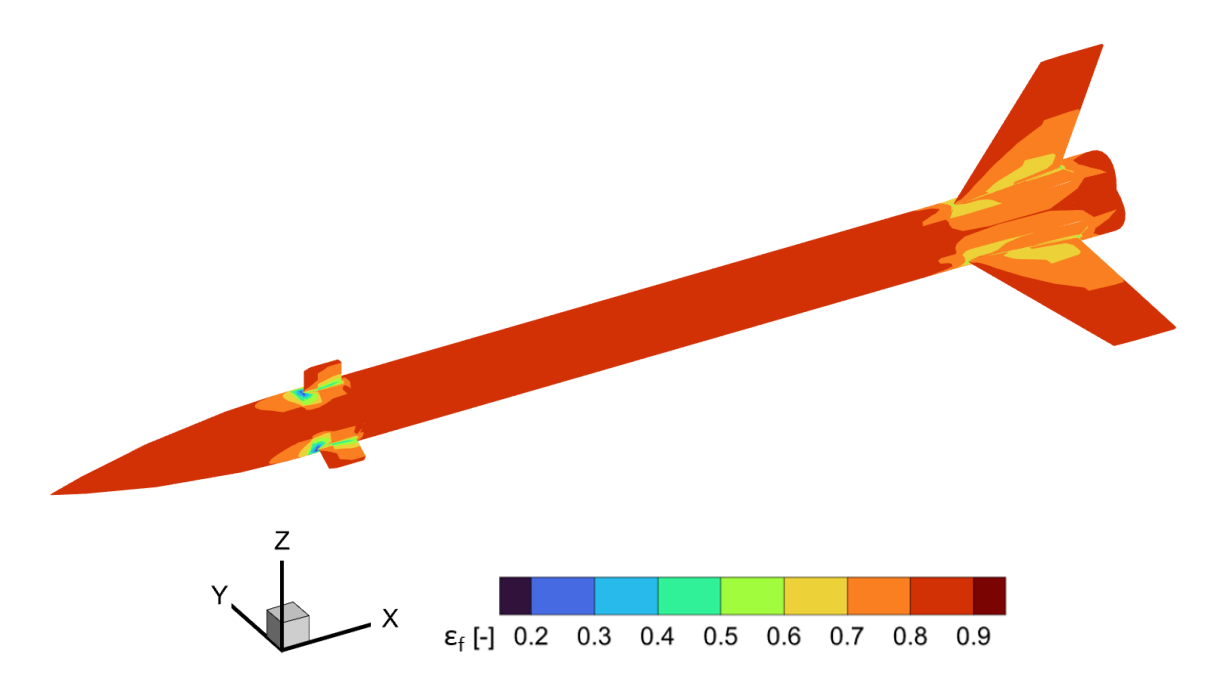


**Fig 3.**  $\varepsilon_f$  contour bands around the vehicle surfaces.

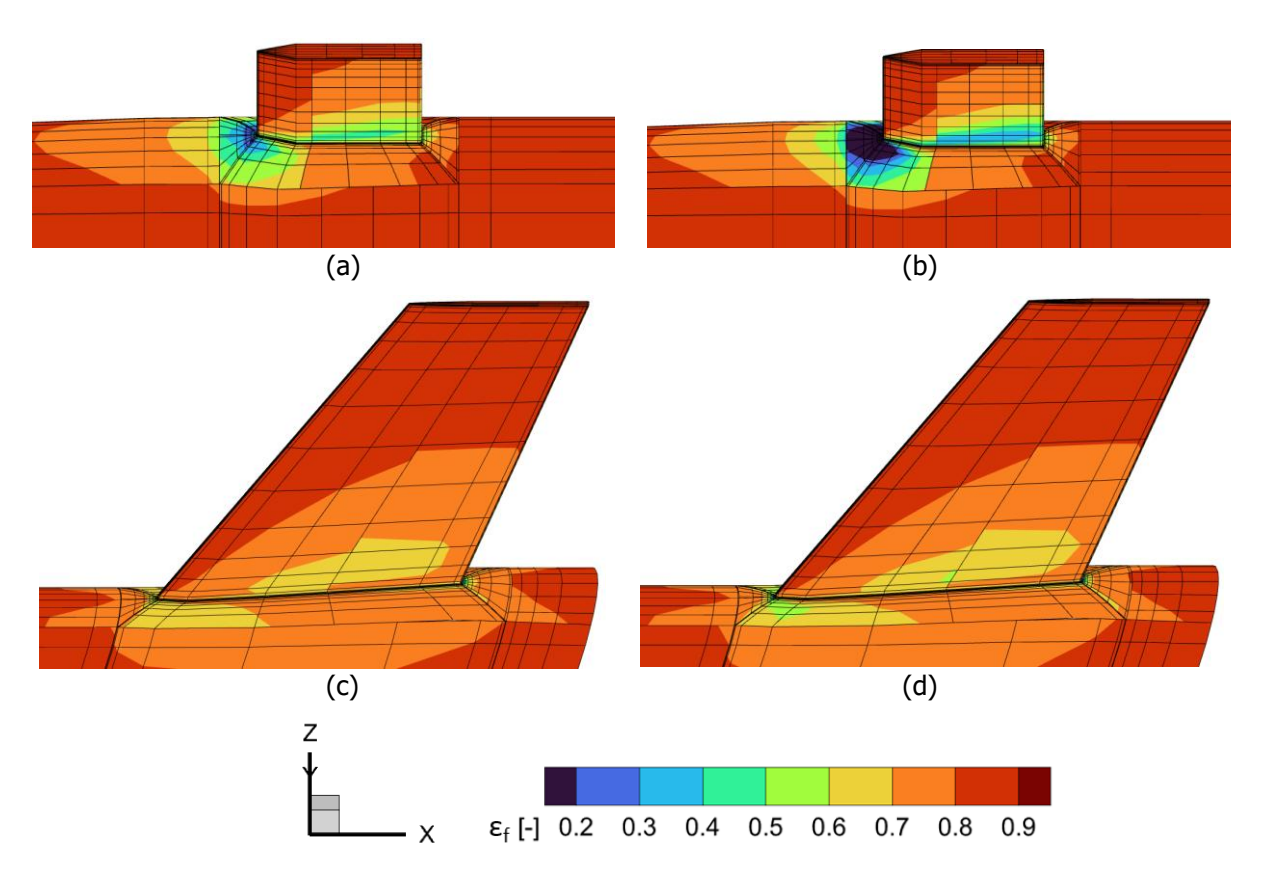


**Fig 4.** Strongly coupled case  $\varepsilon_f$  contour bands are given in (a) and (c) where the  $\varepsilon_f$  distribution is converged during the simulation. (b) and (d) are the outcome of the configuration where the radiation computation is considered only in the final iteration of the simulation.

To capture the increase in temperature at the concave regions due to radiation heating, a reference simulation has been prepared, despite turning off the radiation module GETHRA. Within this reference simulation, the radiation adiabatic boundary condition assumes a reference emissivity  $\varepsilon$  of 0.85 everywhere. The difference between the two simulation cases is as follows: keeping the emissivity  $\varepsilon$ higher in Eq. 4 reveals a lower surface temperature distribution in the reference calculation for the same flow field since the  $q_{\rm gas,w}$  in Eq. 3 is also the same. Nevertheless, it has been known that temperatures on concave region surfaces are higher due to radiation heat exchange. Eventually, the boundary layer temperature distribution is also affected by this surface temperature rise, and the flow field will not be the same. The delta temperature  $\Delta T$  distribution at the vehicle surface is given in Fig. 5, where less than 25 K temperature differences are not shown because of the minor changes in flow fields. The resulting temperature rise in the vicinity of concave regions in Fig. 5 is in agreement with the Fig. 4 provided  $\varepsilon_f$  contour bands. Detailed view of  $\Delta T$  distribution in the vicinity of the canard leading edge shows a temperature increase up to 220 K. Meanwhile the canard side surface close to the vehicle fuselage presents a 130 K temperature variation. Similarly, near the wing leading edge vicinity, a 110 K rise in the temperature is observed. A large wing side surface area is heated 70 K more compared to the reference simulation, where no concave radiation effects considered.

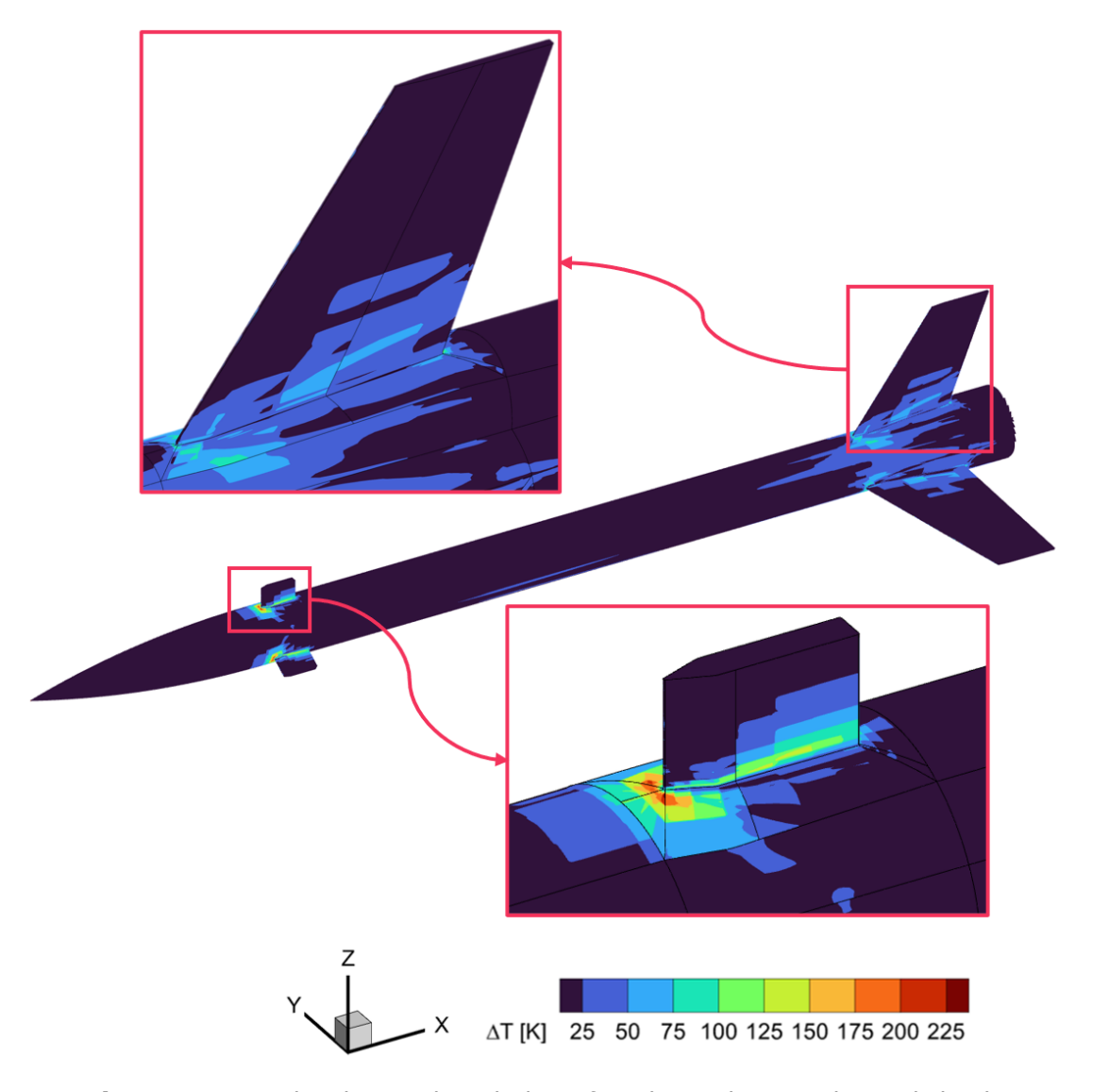


**Fig 5.**  $\Delta T$  contour bands over the vehicle surface due to the strongly coupled radiation computation with respect to the reference calculation, where no radiation heat transfer between concave surfaces is considered.

Computing the vehicle surface temperature distribution enables the infrared signature calculation of the vehicle. Although the emissivity is a function of temperature and wavelength, constant surface emissivity of panels is assumed as 0.85 for this calculation the same as in the GETHRA radiation module. A wide range of infrared wavelengths from 1 to 10 µm is chosen, and Planck's law of radiation is employed. Besides direct irradiation, one-time reflection effects are also considered in the inhouse developed infrared radiation signature computation code. A specific observer panel with a certain radius and area yielding a unit solid angle steradian (sr) is defined for infrared signature computation [14]. Then, the view factors between vehicle surface panels and the observer plane are computed. The right-hand side of Fig. 6 provides two such view factor distribution of vehicle surface panels regarding the observer panel at 0° and 30° configurations. The yellow color in this figure represents a higher view factor value. On the left-hand side of Fig. 6, the radiative intensity polar plot is drawn in consideration of observer plane rotation around the x-axis of the vehicle. Radiation effects in concave regions give rise to the infrared signature up to 2% compared to the reference computation, where no radiation in concave regions is considered.

A further finding is about the importance of vehicle geometry in infrared signature computations. Based on the observer plane angle relative to the vehicle, the computed radiative intensity is changed since the aerodynamic design surfaces, like canards and wings, are also hot and radiating heat energy. The maximum infrared signature of the vehicle is obtained when the observer's viewing direction is orthogonal to the canard and wing side surfaces, such as a 30° rotated configuration.

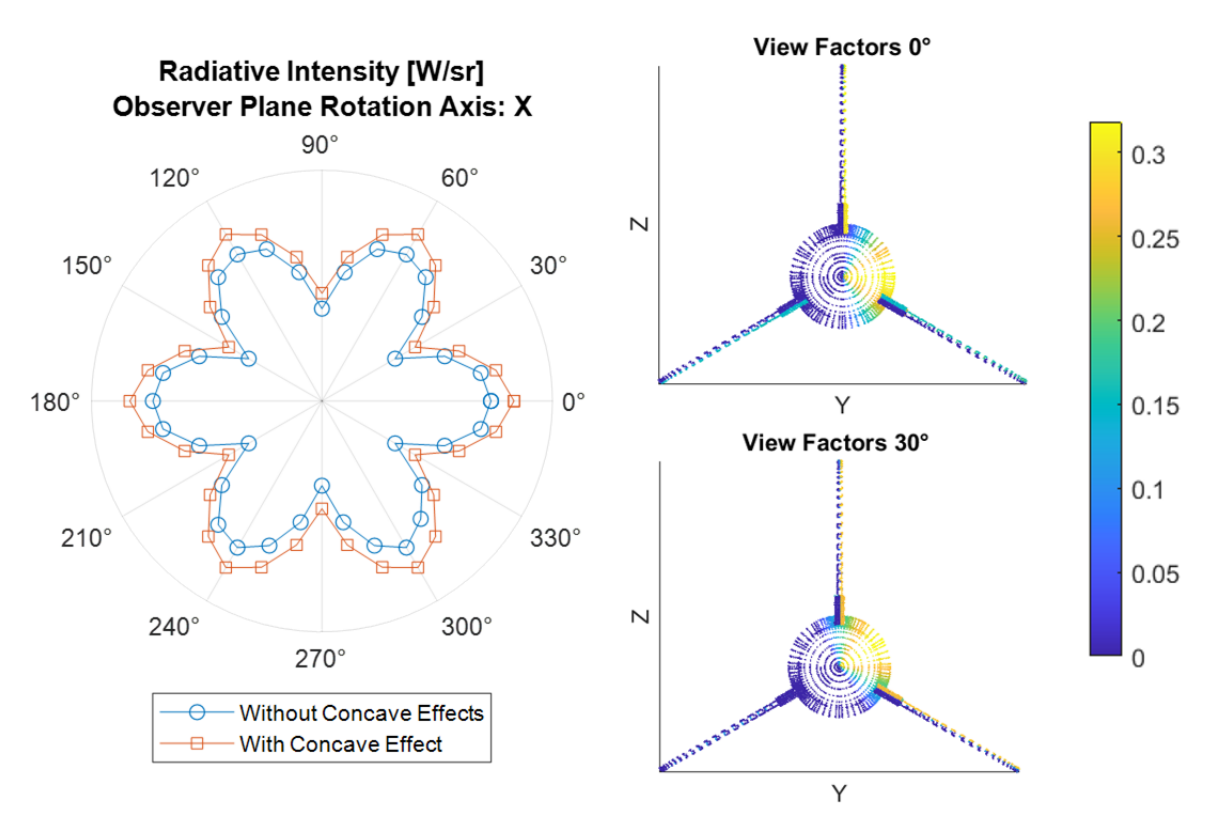


**Fig 6.** Infrared signature polar plot of the flight vehicle rotated around the X-axis, together with example 0° and 30° view factors.

## 4. Conclusion

High-speed flight vehicles in hypersonic regime are exposed to high thermal load due to strong shock formation around the vehicle nose tip, canards, wings, etc. Aerodynamic heating leads to hot vehicle surfaces. The radiation mode in heat transfer gains significance, especially for these hot solid surfaces. Although many hypersonic flight vehicles benefit from radiation cooling, heat is trapped in concave geometry regions of the vehicle where the hot surfaces are directed toward each other. Canard and wing root regions, where they are structurally connected to the vehicle fuselage, are such examples of

the selected vehicle. Within this study, these regions are investigated using the fictitious emissivity approach, which is a distribution over the flight vehicle surface and computed with respect to the reference surface emissivity of the vehicle. More than 200 K temperature rise in the vicinity of concave regions was observed for the selected vehicle. Furthermore, the increase in surface temperature at concave regions of the flight vehicle influences the flow field and even non-concave regions since. At the end, the infrared signature of the selected flight vehicle and the corresponding view factors are provided. Up to 2% increase due to radiation heat transfer near concave regions is calculated. Without considering the radiation heat transfer of solid surfaces, the temperature distribution in the vicinity of the concave flight body exterior is underestimated for a hypersonic flight vehicle thermal analysis.

#### References

- 1. Van Driest, E. R.: The Problem of Aerodynamic Heating. Aero. Eng. Rev., vol. 15, no. 10, 26-41 (1956)
- 2. Bonin, J.: Untersuchung der optischen Abstrahlung von ballistischen Flugkörpern unter Berücksichtigung der Kopplung von Strömung und Strahlung. (Investigation of optical radiation of ballistic spacecrafts considering the coupling of flow and radiation). Dissertation, Universität der Bundeswehr München. (2020)
- 3. Gülhan, A., Hargarten, D., Zurkaulen, M., Klingenberg, F., Siebe, F., Willems, S., Di Martino, G., Reimer, T.: Selected results of the hypersonic flight experiment STORT. Acta Astronautica (2023). https://doi.org/10.1016/j.actaastro.2023.06.034
- 4. Anderson, J.D., Degroote, J., Degrez, G., Dick, E., Grundmann, R., Vierendeels, J.: Computational Fluid Dynamics. Springer, Berlin. (2009)
- 5. Hoarau, Y., Pena, D., Vos, J. B., Charbonier, D., Gehri, A., Braza, M., Deloze, T., Laurendeau, E.: Recent developments of the Navier Stokes Multi Block (NSMB) CFD solver. 54th AIAA Aerospace Sciences Meeting. Reston, Virginia. (2016). https://doi.org/10.2514/6.2016-2056
- 6. Göbel, F., Vos. J., Mundt, Ch.: Simulation of the FIRE II flight experiment. 42<sup>nd</sup> AIAA Fluid Dynamics Conference and Exhibit. Reston, Virginia. (2012). https://doi.org/10.2514/6.2012-3350
- 7. Höld, R.K., Fornasier, L.: Investigation of thermal loads on hypersonic vehicles with emphasis on surface radiation effects. 19th ICAS Congress of the International Council of the Aeronautical Sciences. (1994)
- 8. Liou, M.-S.: A sequel to AUSM, Part II: AUSM+-up for all speeds. Journal of Computational Physics, 137-170 (2006). https://doi.org/10.1016/j.jcp.2005.09.020
- 9. Van Leer, B.: Towards the ultimate conservative difference scheme. II. Monotonicity and conservation combined in a second-order scheme. Journal of Computational Physics, 361-370 (1974). https://doi.org/10.1016/0021-9991(74)90019-9
- 10. Anderson, J.D.: Hypersonic and High-temperature Gas Dynamics. American Institute of Aeronautics and Astronautics, Virginia. (2019)
- 11. Teschner, F.: Numerical Investigation of the Hypersonic Laminar-Turbulent Boundary-Layer Transition around a Blunted Cone in CO2, Mars and Earth Atmospheres. Dissertation, Universität der Bundeswehr München. (2020)
- 12. Menter, F.R.: Two-equation eddy-viscosity turbulence models for engineering applications. AIAA Journal, vol. 32, no. 8, 1598-1605 (1994). https://doi.org/10.2514/3.12149
- 13. Hirschel, E.H.: Basics of Aerothermodynamics. Springer. (2004)
- 14. Howell, J.R., Mengüc, M.P., Daun, K., & Siegel, R.: Thermal Radiation Heat Transfer (7th ed.). CRC Press. (2020). https://doi.org/10.1201/9780429327308